ARTICLE

Correlation of Magnetic Resonance (EPR, ssNMR) Parameters and Crystal-Microstrain in Marbles as a Tool to Probe their Provenance

Loukas Belles[a], Christos Dimitriou[a], Constantinos Moularas[a], Maria Solakidou[a], Marinos Theorodakopoulos[b], Maria Louloudi[b] and Yiannis Deligiannakis[a*]

Marbles constitute a significant family of materials, for antiquities, as well as modern constructions. Herein, we have studied Greek marbles, using Electron Paramagnetic Resonance (EPR) and solid-state Nuclear Magnetic Resonance (ssNMR) spectroscopies, focusing on their structural microenvironment. Spin-Hamiltronian parameters derived form EPR spectra of naturally occurring $^{55}Mn^{2+}$(S=5/2, I=5/2) atoms in marbles were studied as structural probes. EPR data at 300 K provide a library of $^{55}Mn^{2+}$ Zero-Field-Splitting parameters (E, D). The effect of temperature (300 up to 700 K) on $^{55}Mn^{2+}$-ZFS (E, D) and the straind of the D-tentor (D_{strain}) was studied by High-Temperature EPR spectroscopy. The EPR data, combined with ^{13}C-ssNMR, provide deteiled physocichemical information on the calcite and dolomite crystal phases in the marbles. In parallel, we have analyzed the lattice-microstrain (ε_0) of the marbles' crystallites using high-resolution XRD data. Analysis of the correlation between the D-values of Mn^{2+} centers and the (ε_0)-XRD reveals trends that reflect the provenance of the marbles. In this context, we discuss the correlation between {D-values of Mn^{2+} centers and (ε_0) –mirostrain} as a novel tool to probe the provenence of marbles.

1. Introduction

The use of Greek marble in ancient architecture and sculpture has fascinated researchers and historians for centuries[1]. The physiochemical properties of Greek marbles, including their mineral composition, texture, and color, have made them a subject of intense study in the field of material science[2,3]. Identification of the origin of marbles used in monuments is very important[3]. Moreover, the effects of environmental factors such as temperature and mechanical stress, if properly measured and analyzed, are expected to provide insights into their historical evolution[1]. In fact, it is well recognized that the precise attribution of geographical origin and environmental fingerprints to ancient marbles can provide useful information about cultural linkages[3–5]. A closely related task is to establish scientific tools that allow to interlink parts or fragments from monuments, that have been shattered or separated[6]. In this context, so far, the characterization of marbles and the determination of their provenance constitute important archaeological challenges that require use of specific petrographical and physicochemical techniques[7]. Marble is defined as a carbonate rock that has undergone regional or contact metamorphism, according to petrography[4], in which calcite [$CaCO_3$] or dolomite [$CaMg(CO_3)_2$] compose its crystal lattice[8]. Apart from calcite or dolomite, which are the structural minerals, marble can also contain trace amounts of accessory minerals such as quartz, aluminosilicate minerals (muscovite, chlorite, phlogopite, etc.), and in some cases, Fe-oxides and graphite, giving veins of orange or dark color, respectively[9]. Calcite and dolomite are responsible for the typical white color of marble, while impurities and other minerals often contribute to different colors, which vary from white to blue, gray, or even black[10,11]. The whiter the marble stone, the lower the accessory mineral content, and this renders their distinction more difficult. Thus, white marbles are among the most difficult to differentiate with regard to their origin, i.e., due to their broad use in antiquity and lack of distinguishing macroscopic characteristics[3,5,6].

Calcite is a calcium carbonate with a trigonal crystal structure. Insertion of divalent cations, such as Mg^{2+}, Mn^{2+}, Fe^{2+} and Fe^{3+} create defects in calcite microstructure[12]. Thus, techniques such as Instrumental neutron activation analysis (INAA)[13], trace element analysis[14], analysis of stable-isotope ratios using mass spectroscopy[15], cathodoluminescence[16], X-ray diffraction (XRD)[17], have been utilized as high -resolution tools to analyze composition, structure, and ultimately the origin and geochemical itinerary of white marbles. Magnetic resonance spectroscopies, i.e. electron paramagnetic resonance (EPR)[6,8,18] solid-state NMR (ssNMR) spectroscopy[19] can offer high-precision, high resolution information on the local environment of the marble structures. For example, ^{13}C-ssNMR for calcite identified crystal flaws as well as the presence of trace elements, establishing the origin of marble[19]. In a more recent study, in addition to ^{13}C, two extra nuclei, i.e., ^{25}Mg-ssNMR and ^{43}Ca-ssNMR, were shown to provide specific information on

a. *Laboratory of Physical Chemistry of Materials & Environment, Department of Physics, University of Ioannina, 45110, Ioannina, Greece.*
b. *Laboratory of Biomimetic Catalysis & Hybrid Materials, Department of Chemistry, University of Ioannina, 45110 Ioannina, Greece.*
† Footnotes relating to the title and/or authors should appear here.
Electronic Supplementary Information (ESI) available: [details of any supplementary information available should be included here]. See DOI: 10.1039/x0xx00000x

variations among dolomitic marbles that can assist in their discrimination[20]. It should be underlined, however, that a combination and correlation of information is necessary, not a single technique, to address the complex issue of marble provenance and geochemical itinerary[21-24].

Herein, we propose a methodological approach based on concurrent use of magnetic resonance (EPR and ssNMR) together with high-resolution XRD to establish a methodology that will contribute to the analysis of white marble microstructure and their provenance identification. Previously, Maniatis *et al.*[22] and Mandi *et al.*[18], conducted more in-depth and systematic research on the EPR spectrum of marble. Their findings were subjected to hierarchical aggregative cluster analysis, and 170 marbles constituted the first EPR database[18]. Up today, this database has been extended significantly[5,9,23], and a considerable number of archaeological marbles have been analyzed, with encouraging results[2,4,14,24].

The underlying solid-state physics basis of these EPR-based information, is as follows: EPR identifies Mn^{2+} and Fe^{3+} in substitution of Ca^{2+} in the $CaCO_3$ of aged marble's surface[9]. Because the radius of Mn^{2+} (0.91 Å) is closer to that of Ca^{2+} (1.00 Å), it fits more easily into the calcite lattice without causing considerable disturbance. In contrast, Fe^{3+} (0.67 Å) generates far-greater crystallographic distortion and tends to access non-lattice locations in calcite rather than substitutional sites[25]. Re-crystallization results in the formation of freshly produced calcite crystals, which are anticipated to have lower impurity concentrations than marble crystals[26]. Water penetration induces re-crystallization but also enables Mn^{2+} and Fe^{3+} to enter marble surfaces in various oxidation states in clay minerals[27]. Additionally, the presence of fungus or bacteria promotes the entry of water and crystal dissolution, in addition to microbial oxidation or reduction of Fe and Mn on marbles' surfaces[28].

Hereinafter, our working hypothesis was that all those geochemically or environmentally induced micro-alterations of the marble structures could provide a correlating fingerprint of the marble's provenance. On this front, we focus on the study of local micro-alterations in marble crystals by combining EPR, ss-NMR, and XRD. In contrast to the classical use of XRD[17,29,30] i.e. as standard method for crystal-phase identification in

marbles, herein we elaborated on high-resolution analysis of the XRD focusing on the analysis of the microstrains of the crystallites[31]. Recently Yakaboylu *et al.*[31] have reported that strain analysis can provide distinct information on Marcellus Shales. Hereafter, our method relies on the assessment of structural-microstrain by two methods, (see conceptual Figure 1 and 2): [i] X-Ray-Diffraction line-broadening and [ii] Zero-Field-Splitting (ZFS) tensor [32] from EPR spectra of Mn^{2+} centers, naturally occurring into the marbles. The full details of the two methods and the definitions of the parameters are provided in Section 2.1, hereafter.

In brief, we define lattice-microstrain, as an inhomogeneity of the lattice parameters, i.e., the unit cell vector's alterations, with no change in the XRD diffraction angle position (Figure 1), i.e., no change on the average distance of the calcite or dolomite Miller planes *{hkl}*, see more explanation in Figure 1. In this context microstrain analysis through X-ray diffraction (XRD) provides information on the examination of the displacements of lattice-atoms from their ideal positions within a crystalline material. This provides valuable insights into the level of lattice distortions within the marbles, aiding in the understanding of their mechanical properties, durability, and potential susceptibility to environmental factors.

The EPR signals from the $^{55}Mn^{2+}$ (S = 5/2, I = 5/2) ions provide valuable information about their concentration and local environment, contributing to a deeper understanding of the composition and origin of the marbles[22]. Zero Field Splitting (ZFS) is a phenomenon that arises from the interaction between electron-spins in atoms with more than one-unpaired electron[33] i.e. $^{55}Mn^{2+}$ has five-unpaired electron, thus S = 5/2. Moreover, the isotope ^{55}Mn has 100% natural abundance and is characterized by I = 5/2. Thus, the S = 5/2 and I = 5/2 of $^{55}Mn^{2+}$ provide a highly sensitive spin-probe system that sheds light on its immediate structural environment[34]. By analyzing the ZFS-tensor D (fully detailed in section 2.1) of marbles by EPR spectroscopy, we can gain insights into the atomic-level characteristics of the materials, such as the orientation of the magnetic-tensors and the distribution of the principal values of the D-tensor, that we define as D_{strain}, see more explanation in Figure 2. Our key-hypothesis was that the ZFS-tensor D values and as D_{strain} can act as sensitive probes of variation of the local
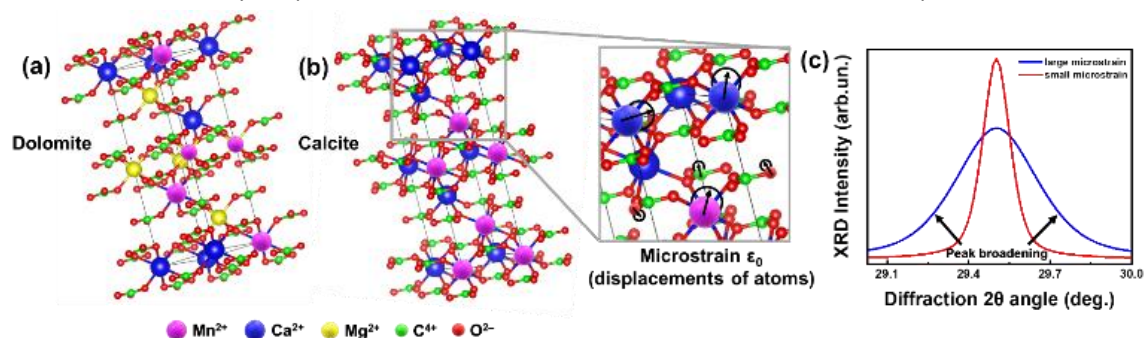

Figure 1. Concept of microstrain analysis with use of XRD. (a) The unit cells of the predominant phases in Greek marbles, i.e. calcite ($Ca(CO_3)$) and dolomite ($CaMg(CO_3)_2$). (b) Magnified region of calcite's unit cell demonstrating the displacement of atoms. The degree of this relocation is captured by the microstructural (ε_0) analysis utilizing XRD and TOPAS software. (c) Theoretical XRD pattern of a crystallite when has small (red line) and large (blue line) microstrain. We underline than, since the size of the marble crystallite is in the *micro*meters range, see data in Table 4, the observed XRD-broadening in *not* due to nano-size effects, but exclusively due to lattice-strains.

microstructure among various homologous marble materials i.e., reflecting their geochemical history and provenance.

In this context, herein we used in tandem Electron Paramagnetic Resonance (EPR) spectroscopy and X-Ray Diffraction (XRD) to study on a systematic-comparative basis a family of white marbles from various regions in Greece, see the map in Figure 3. In addition, we have used high-temperature EPR[35] ias advanced non-conventional EPR technique to study the Mn^{2+}-ZFS in marbles *in-situ* at elevated temperatures up to 700K. This allowed us to investigate the possible role of temperature-induced strains in the materials and distinguish it from its interference with its geochemical EPR fingerprint.

Overall, the key aims of the present work where: [i] to present a comprehensive correlation analysis of the structural, spectroscopic, magnetic properties of various types of Greek marbles, including their crystal structure, lattice-microstrain and $^{55}Mn^{2+}$ Zero-Field-Splitting tensor strain. [ii] to propose the concurrent use of High-Resolution-XRD and EPR as a novel methodological protocol to address questions of provenance, thermal, geochemical history of marbles.

2. Experimental Methods

2.1 Description of microstrain-analysis methods using XRD and EPR

The prevailing crystal phases for marbles are calcite [Ca(CO3)] and dolomite [CaMg(CO3)2]. Their unit cells are depicted in Figure 1a. The relocations of atoms from their ideal positions within the Ca(CO3) lattice (Figure 1b) lead to the XRD peak broadening, with no-shift of the Bragg-diffraction angles. Microstrain represents displacements of atoms from their ideal positions, generated by any lattice imperfection (dislocations, vacancies interstitials and similar defects), Equation 1. It can be conceived by considering two extreme values of the lattice spacing d, namely d+Δd and d−Δd, where $\varepsilon_0 = \Delta d/d$ is attributed

with $\beta_{FWHM}(str)$ representing the full-width-at-half-maximum of the XRD-peak related to microstrain broadening. Thus, the larger the microstrain, the larger the XRD-peak broadening. (Figure 1c). We underline than, since the size of the crystallite is nor altered i.e. typically in marbles is in the *micro*meters range, see data in Table 4, the observed XRD-broadening in *not* due to nano-size effects, but exclusively due to lattice-strains.

Herein we have used high-resolution detection of the XRD signals, with angular steps 0.01 degrees, and use of TOPAS[37] software, to implement Rietveld analysis, microstructure analysis. The concept of microstrain (ε_0) entails the deviations of atoms from their equilibrium positions within a crystal lattice, which are generated by different lattice imperfections such as dislocations, vacancies, interstitials, and similar defects[38]. By analyzing the broadening and shifting of diffraction peaks in the XRD pattern using TOPAS, the magnitude and distribution of microstrain in calcite and dolomite crystals can be quantitatively assessed.

The Zero Field Splitting tensor (D-tensor) has three principal values (D_x, D_y, D_z) in its principal-axes system [32,33] see Figure 2a. The $D_{x,y,z}$ values are influenced by the electron-electron interactions within the $^{55}Mn^{2+}$ atom, which in-turn are influenced by the immediate chemical environment of the atom[23,33,34]. Typically, the $D_{x,y,z}$ values are influenced by factors such as ligand field strength, crystal symmetry, and local distortions[32,34]. These changes in D can be traced by EPR spectra i.e., see examples of numerically simulate EPR spectra in Figure 2b. Importantly, as we exemplify in Figure 2b, D_{strain} can be reliably traced by EPR spectroscopy *via* alteration of certain spectral features e.g. the high-field transitions.

In this way, we have quantified and analyzed the lattice-microstrain (ε_0) by XRD and the ZFS, (D_{strain}), by EPR based on the definition and conventions defined herein.

2.2 Preparation of Marble Materials

The marble samples were collected as raw materials from different quarries in Greece, according to their historical
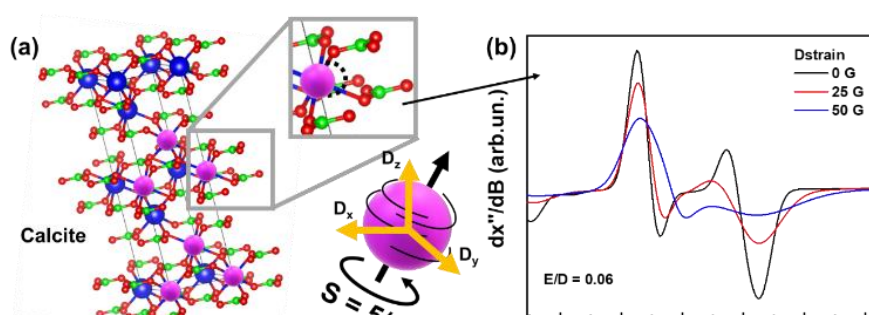

Figure 1 Phase composition of all collected Greek marbles contain calcite and dolomite. (a) Calcite unit-cell of any marble , generated using VESTA software[36], where we present a local displacement of Mn^{2+} in the lattice and therefore the strain which can be described as D_{strain} (orange arrows) versus the spin tensor (black arrows) direction. (b) EPR spectra which have different D distribution which displays the changes of linewidths according to D_{strain} value.

as the mean deviation

$$\varepsilon_0 = \frac{\Delta d}{d} = \frac{\beta_{FWHM(str)}}{4\tan\vartheta} \qquad \text{Equation (1)}$$

locations and their color, choosing from a colorful palette of Greek marbles that were used by many artists all over the centuries. In Figure 3, we present a map of the regions where marbles were collected from. Marbles of different colors (Marble #2 (Ioannina) yellowish, Marble #6 (Chios Island) dark grey, Marble #4 (Thassos island) white and different historic

importance, i.e., Marble #1 from Naxos Island and Marble #4 from Thassos island are those two of great importance due to their large use in great monuments and sculptures.
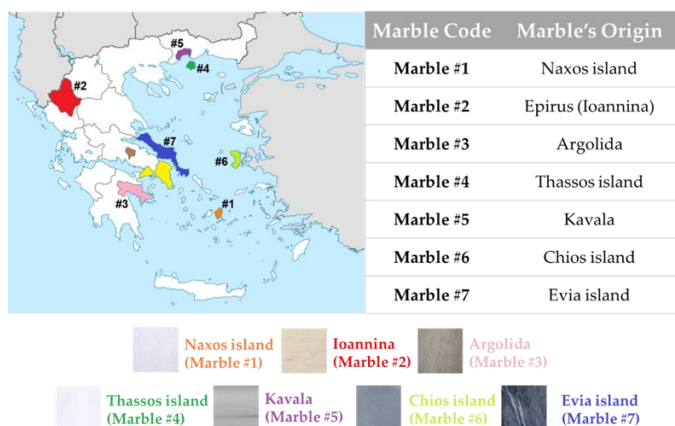

Marble Code	Marble's Origin
Marble #1	Naxos island
Marble #2	Epirus (Ioannina)
Marble #3	Argolida
Marble #4	Thassos island
Marble #5	Kavala
Marble #6	Chios island
Marble #7	Evia island

Naxos island (Marble #1) Ioannina (Marble #2) Argolida (Marble #3)
Thassos island (Marble #4) Kavala (Marble #5) Chios island (Marble #6) Evia island (Marble #7)

Figure 2 Map with selected colored locations, from where marbles were collected. The Greek marbles were collected according to their color and historic importance.

Firstly, the collected marbles were cleaned up, by soft-tissue wiping, so that dirt and surface weathering were removed appropriately. Afterwards the marbles were crushed to coarse powder of millimeter-size to avoid artefacts induced by the treatment. Comparison with intact pieces shows that coarse-powders did not have additional treatment-induced signals. Therefore, the marbles used through all experiments for EPR, ssNMR and XRD analysis were in coarse-powder form.

2.3 Material Characterization Methods

Electron Paramagnetic Resonance: First, room temperature (300K) or 77K (liquid N2) EPR spectra of marbles were recorded with a Bruker ER200D spectrometer, using a perpendicular-mode cavity model Brucker-ER4102ST. 15mg samples were prepared and placed in 5 mm diameter quartz tubes, Suprasil Willmad. The experimental conditions were: modulation amplitude = 10 Gpp; modulation frequency = 100 KHz; T = 300 K and 77 K for iron ions, see Figure S.1., microwave power = 20 mW; microwave frequency: 9.53 GHz.,

High Temperature EPR spectroscopy: High temperature EPR spectra were recorded with the Bruker ER200D spectrometer and a high temperature cavity model Brucker-ER41114HT. The powder samples were inserted into the high-T cavity using special zirconia-glass tubes obtained by Brucker. The experimental conditions were: modulation amplitude = 10 Gpp; modulation frequency= 100KHz, microwave power=5mW, microwave frequency= 9.57GHz. The temperature was increased from T=300 K up to 700K±0.1K by a digitally controlled hot-N$_2$ gas flow, the heat control was achieved via a Brucker BVT3000, a BVTB3500 and monitored *in situ* in the ER41114HT cavity by a type K thermocouple which is placed under the sample. At each temperature the sample was allowed to equilibrate for at least 60 minutes and its spectral evolution was recorded. To verify the effect of long term thermal exposure, we have heated samples for up to 3 days in a lab-furnace. We

found that within 30 minutes the EPR spectrum attained a steady-state form at all temperatures. The g-values were calibrated using DPPH as spin standard (g = 2.0036 ± 0.0003) [39].

Theoretical Simulation of $^{55}Mn^{2+}$ (S = 5/2, I = 5/2) EPR spectra: Numerical simulations of the EPR spectra were conducted using EasySpin, under MATLAB [40].
$^{55}Mn^{2+}$ spectra states with S=5/2 and I=5/2 were simulated using the Spin Hamiltonian, Equation 2 [41]

$$\widehat{H} = \beta \vec{B} \hat{g} \vec{S} + \vec{S} \widehat{D} \vec{S} + \vec{I} \widehat{A} \vec{S} \qquad \text{Equation (2)}$$

where the first term is the Zeeman energy, the following two are the ZFS (zero-field splitting) interaction determined by D and E, the axial and rhombic zero field splitting tensor parameters respectively, the last term is the hyperfine interaction of the ^{55}Mn (I = 5/2).

Solid state NMR (ssNMR): The collected marbles were powdered with an agate mortar to obtain 190 ± 5 mg to fill the 4 mm-diameter Cross Polarization Magic Angle Spinning (CP-MAS) zirconium oxide rotor. The ^{13}C spectra were obtained on a 400 MHz Bruker Avance II spectrometer equipped with the CP-MAS probe. The spectra were collected at the Department of Chemistry at the University of Ioannina. The rotation rate of the spin was at 8000 Hz for all the experiments, a single one-pulse sequence using 90° nutation angle of 4 µs, a relaxation delay of 300 s and 256 scans. Two dummy scans were used to ensure a reproducible pre-saturation of the signal. For all the marbles, the measurement conditions (D1 at 300 s, number of scans at 256, dummy scans 2 and receptor gain at 512), the material mass was (190 ± 5 mg) in all cases. Marble #1 was measured by incorporating with adamantane ($C_{10}H_{16}$) as a chemical shift standard for solid-state NMR. This signal was used to calibrate all NMR signals for all measured marbles.

X-Ray Diffraction (XRD): The crystal structures of the materials were analyzed by XRD in a Bruker-D8 Advance diffractometer (Cu Ka radiation λ = 1. 5406 Å, 40 kV, 40 mA) at 2ϑ = 10°–130° (step size of 0.01° at a rate of 0.6 s per step). The average crystallite size was calculated by the Scherrer equation (Equation 3):

$$d_{XRD} = \frac{K \lambda}{FWHM \cos \vartheta} \qquad \text{Equation (3)}$$

where d_{XRD} is the crystallite size (nm), k is a shape constant (in this case 0.9), λ is the wavelength of Cu Kα radiation (1.5406 Å), *FWHM* is the full width at half maximum and ϑ is the peak-diffraction angle.

3. Results and Discussion

EPR and H.T. EPR

Figure 4a, presents broad scan 77K EPR spectra of all marbles. In all cases, EPR spectra characteristic of $^{55}Mn^{2+}$(S = 5/2, I = 5/2) are detected[34]. A typical $^{55}Mn^{2+}$ EPR spectrum is characterized by six main peaks, corresponding to the allowed 2I + 1 hyperfine splitting of -1/2 up to 1/2 transitions. Between each hyperfine, a pair of 'forbidden' $\Delta M_I = 2$[34] peaks are present. As analyses originally be Reed and Markham their relative intensity and line shape reflect the numerical values of the components of tensors **D** and **A**[34]. In marble structures, all these factors depend on the type of marble, its geological history, and the location of the marble[4,5,6] . The EPR spectra in Figure 4 are due Mn^{2+} ions occupying Ca-sites, in the unit cells of calcite or dolomite, see Figure 2a. The black-dashed lines in Figure 4a are theoretically calculated $^{55}Mn^{2+}$ EPR spectra, using the
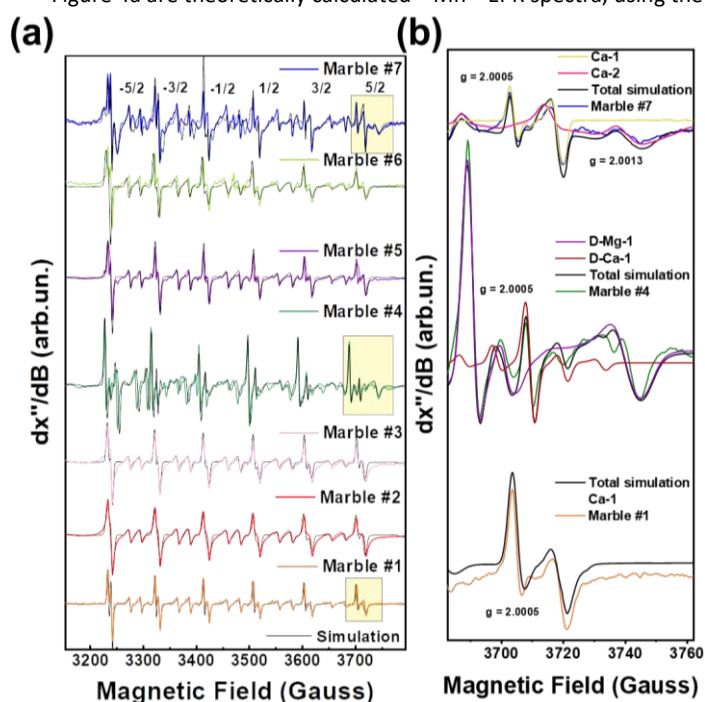

Figure 3(a) 77K EPR spectra of all marble marbles. Due to traces of divalent manganese in substitution of some calcium or magnesium atoms in the lattice six double peaks are presented in the experimental. The EPR spectra were simulated via Hamiltonian quantification. *Experimental conditions*: Modulation Amplitude 10 Gpp, microwave power 32 mW, modulation frequency 100 KHz. **(b)** A selected range of EPR spectra was used to determine the different peaks and connect them with Ca and Mg-atoms.

Spin Hamiltonian parameters listed in Table 1. Noticeably the hyperfine tensor anisotropy of all marbles did not vary significantly despite the different phase composition.

In Figure 4b, we exemplify EPR spectra, from marbles #1, #4, #7 that show significant differences. Such analysis, see Spin-Hamiltonian parameters in Table 1, provides two pieces of information: [i] the hyperfine-tensor A values of the $^{55}Mn^{2+}$ (I = 5/2), and [ii] the D-tensor parameters together with its D$_{strain}$ values. Accordingly, marble #7 shows two EPR spectral components corresponding to two types of Mn-atoms. Marble

#7 is pure calcite. Based on literature data [42,43], the two Mn-atoms occupy two different Calcium-cites in the calcite structure, marked Ca-1 and Ca-2, in Figure 4b. As seen in Table 1 these two species are distinguishable by their different g-values, **D**-tensors, and **A**-tensors. Site Ca-2 is characterized by smaller-D-tensor values and lower D$_{strain}$ i.e., 4 *vs.* 18 for Ca-1 site.

Table 1. Spin Hamiltonian parameters for pristine Greek white marbles (#1-7).

Temperature (K) ($\pm$ 1)	A [A_x, A_y , A_z] (Gauss) ($\pm$ 1)	[D, E] (Gauss) ($\pm$ 0.5)	D$_{strain}$ (Gauss) ($\pm$ 1)	g ($\pm$ 0.0001)
Marble #2				
300	[95, 94, 93]	[86.0, 4.3]	23	2.0005
400	[96, 94, 93]	[81.5, 4.4]	28	2.0005
500	[95, 94, 92]	[80.8, 4.6]	26	2.0005
600	[95, 94, 92]	[110.1, 4.5]	32	2.0005
700	[95, 94, 92]	[94.2, 4.3]	42	2.0005
Marble #4				
300	[94, 95, 96]	[5.4, 0.1]	10	2.0005
400	[95, 95, 95]	[5.6, 0.1]	14	2.0005
500	[95, 95, 95]	[5.8, 0.1]	16	2.0005
600	[95, 95, 95]	[5.3, 0.1]	17	2.0005
700	[95, 95, 95]	[5.5, 0.1]	20	2.0005
Marble #5				
300	[93, 96, 93]	[82.0, 4.6]	12	2.0005
400	[95, 95, 94]	[90.9, 4.6]	17	2.0005
500	[94, 95, 94]	[86.3, 4.6]	21	2.0005
600	[93, 95, 94]	[88.9, 4.6]	30	2.0005
700	[93, 95, 94]	[93.3, 4.6]	40	2.0005
Marble #6				
300	[94, 96, 94]	[90.0, 3.6]	28	2.0005
400	[94, 94, 93]	[87.8, 3.6]	29	2.0005
500	[94, 94, 93]	[88.3, 3.6]	30	2.0005
600	[93, 94, 93]	[96.2, 3.6]	38	2.0005
700	[94, 94, 93]	[92.8, 3.6]	47	2.0005

There specific Spin-Hamiltonian parameters are responsible for the clear differences seen in the EPR spectrum of marble #7, and, as we show in the following, can serve as fingerprints together with the XRD macrostrain parameter (ε_0). On going to marble #4, with a different phase composition, i.e. both calcite and dolomite see XRD data Table 4, we see that its ^{55}Mn-EPR spectrum can be deconvoluted to two sub-spectra, see Table 1 based on literature data[21–23], one ^{55}Mn-type (D-Mg-1 in Figure 2b) refers to ^{55}Mn atoms occupying Mg-atom sites in dolomite, while D-Ca-1 in Figure 2b, corresponds to ^{55}Mn atoms occupying Ca-atom sites in dolomite. Both sites show moderate D$_{strain}$ values 10 and 15 respectively see Table 1. Marble #1 which is pure calcite, shows a single EPR signal, see Table 1, from ^{55}Mn atoms occupying a Ca-atom site, see Ca-1 in Figure 2b. Marble #1 has a high D$_{strain}$ of 21, see Table 1.

Based on the data of Table 1, hereafter we discuss four of them, according to their distinct phases' compositions: marbles #2, #5, #6 have in higher percentage the calcite phase, in comparison with #4 with dolomitic phase. The D$_{strain}$ of these marbles spans a wide range of 10 up to 28 for Ca-sites and 15 for Mg-site in the dolomitic marble #4. We underline that the Hyperfine tensor anisotropy of all marbles did not vary significantly despite the different phase composition.

In addition to the EPR analysis of pristine materials, the selected marbles #2, #4, #5, #6 were studied at our High-Temperature EPR spectrometer (see EPR spectra in Figure S.2 a-d of the Supporting Information).

The protocol was as follows: for each material EPR spectra were recorded *in-situ* for temperatures up to 700 K, under an equilibration time of 2 hours for each temperature. After measurements the marbles were left for 4 hours to cool at room

between the D_{strain} trends for #2, #5, #6 and their distinction vs. marble #4, might be correlate with the [calcite/dolomite] phase ratio: for example, the dolomitic (calcite/dolomite = 3/96), marble #4 with low-initial D and D_{strain}, is more resistant to
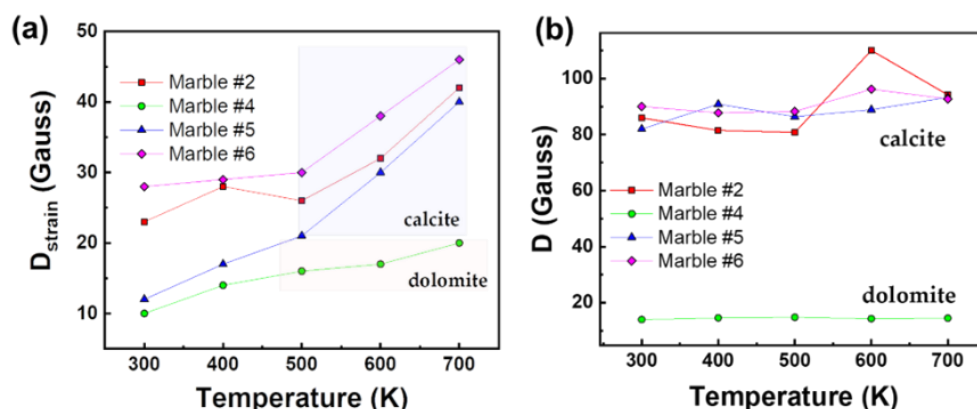

Figure 4 Variations of (**a**) D_{strain} *vs* temperature and (**b**) ZFS (D-tensor) vs temperature, for marbles #1, #2, #3, #4.

temperature 300K and measured again (Figure S.3 a-d). In Table 2, we present the Spin Hamiltonian parameters derived from theoretical simulation of all experimental spectra for all marbles. For simplicity we discuss only the Ca-sites. The trends in D-parameters and the D_{strain} can be visualized in Figures 5a and 5b respectively, where we observe: [i] minor changes on the D-values for all marbles. Same is for the rhombicity parameter E, see Table 2. [ii] a significant increase of D_{strain} at increasing temperatures for all marbles. [iii] the D_{strain} increase was always more prominent in the calcite-sites than in dolomite sites.

distortions at higher temperatures. On the other hand, marbles #2, #5, #6 with mostly calcite phase composition show increased values on both D_{strain} and D values, and D_{strain} sensitivity under thermal stress[44].

To further peer into the microstructural features of these materials, #2, #4, #5 and #6, we have studied their long-term exposure at 700 K: 30 minutes, 3 hours and 3 days. The XRD and EPR data presented in Figure S.4 and Figure S.5, respectively, and the strain-trends vs. calcination time are listed in Table S.1 and Table S.2. The plot of microstrain *vs* the heating time (Figure S.6 and S.7) shows that: in the first 3 hours an important strain increase occurs, while a minor changes up to 3 days.

Table 2. Spin Hamiltonian parameters for the marbles (#2, 4, 5, 6) at variable temperatures (300-700 K)

Marble	g (± 0.0001)		[D, E] (Gauss) (± 0.5)			D_{strain} (Gauss) (± 1)		[A_x , A_y , A_z] (Gauss) (± 1)	
	Ca-site	Mg-site	Ca-site	Mg-site		Ca-site	Mg-site	Ca-site	Mg-site
#1	2.0004	–	–	[90, 5.4]	–	–	21	–	–	[94, 94, 93]	–	–
#2	2.0005	–	–	[86, 4.3]	–	–	23	–	–	[95, 94, 93]	–	–
#3	2.0005	–	–	[82, 5.3]	–	–	18	–	–	[95, 95, 93]	–	–
#4	2.0005	–	2.0005	[5.4, 0.1]	–	[160, 5.4]	10	–	15	[94.5, 95, 96]	–	[93, 93, 90]
#5	2.0005	–	–	[82, 4.6]	–	–	12	–	–	[93, 96, 93]	–	–
#6	2.0005	–	–	[90, 3.6]	–	–	28	–	–	[94, 96, 94]	–	–
#7	2.0005	2.0013	–	[107, 8.9]	[86, 5.4]	–	18	4	–	[88, 99, 95]	[95, 94, 93]	–

Therefore, the present data exemplify that high-temperature Electron Paramagnetic Resonance (EPR) provides a new-powerful to unravel microstrain trends in marbles. As shown in Figure 5a an interesting fact is that, upon increase of temperature all marbles show an increase to D_{strain} parameter, while D does not change. More specifically, marble #5 showed the most significant D_{strain} increase i.e., 70% on heating from 300 to 700 K. Marble #6 also showed a significant D_{strain} increase 39%, marble #2 with an increase of 45%. Marble #4 with the lower D_{strain} value showed an increase of 49%. Noticeably, a more careful perusal allows us to observe that the similarities

^{13}C-Solid-State NMR

Figure 6 shows selected part of the ^{13}C-NMR spectra, (from 171 ppm to 165 ppm), the full spectra are shown in Figure S.8. In Figure 6, we can decipher three parameters: the peak-position (δ in ppm), its width at half maximum (Δν1/2), and the integrated area of the resonance (Table S.3). The δ (ppm) and Δν1/2 values are listed in Table 3. The calibrated δ-values show rather small variations around 167-168 ppm that is assigned to ^{13}C of structural carbonates[45]. These structural carbonates in dolomite [$CaMg(CO_3)_2$], or calcite [$Ca(CO_3)$], is clearly distinct

from free carbonates that is typically detected at is at 170.5 ppm.[20] The linewidths ($\Delta v_{1/2}$) listed in Table 3, vary in the range 32.4 to 60.6 Hz depending on the marble.The carbonate peak broadening ($\Delta v_{1/2}$) may be caused either from the different distribution of the carbonates due to the presence of other atoms like Fe, Mn, Mg, which can substitute Ca in the crystal lattice of calcite, or/and due to the presence of para/ferromagnetic substances/impurities[46]. From Table 3, marble #4 has the highest percentage of dolomite with few ferro/paramagnetic impurities (see Table 4).

Table 3. ^{13}C solid state NMR spectral characteristic for the Greek white marbles.

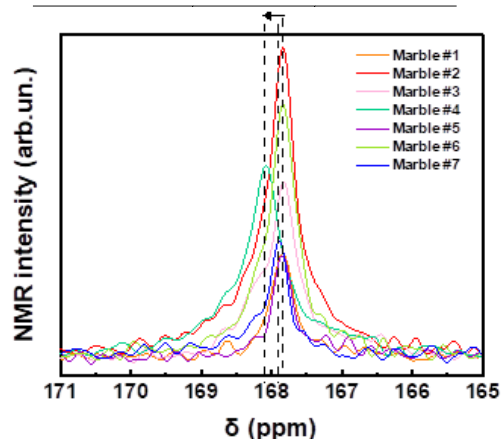| Marble	δ (ppm)	$\Delta v_{1/2}$ (Hz)
#1	167.83	39.6
#2	167.83	47.5
#3	167.82	54.2
#4	168.07	60.7
#5	167.84	32.5
#6	167.83	46.9
#7	167.88	33.2

Figure 6 ^{13}C NMR spectra of all marbles magnified in the carbonate's region.

This material shows that higher $\Delta v_{1/2}$=60.6Hz and ^{13}C δ shift. We see that these ^{13}C-strains are correlated with the highest structural macrostrains ε_0 i.e., see XRD data in Table 5. Noticeably the dolomitic marble #4 shows the lowest D and D_{srtain} values of ^{55}Mn centers. All other marble marbles have almost the same δ-ppm and lack of dolomite phase. Marble #2 and #6, have Fe^{3+} ions and lastly marbles #1, #5 and #7, having the lowest concentration of ions in their structure.[47] Overall, the ^{13}C-NMR data provide additional information on the microstructure of the studied marbles. We underline that EPR, NMR and XRD probe different aspects of the marble structure, therefore, not a single method can provide material-discriminating information alone. As we show in the following, the correlation of the trends of the parameters allows a better material-discriminating strategy to be built up.

Lattice-microstrain probed by X-Ray Diffraction

The XRD patterns for all marbles are presented in Figure 7a. As expected, they show that the predominant phases are calcite

($CaCO_3$) and dolomite ($CaMg(CO_3)_2$), with traces of quartz, magnetite, akermanite and ankerite. All the observed diffraction peaks can be indexed as the $CaCO_3$ with face-centered rhombohedral cell with trigonal symmetry (3̄m), a = 5.01 Å, b = 5.01 Å, and c = 16.99 Å (JCPDS Card No. 86-2340). The peaks at 23.06°, 29.44°, 31.43°, 35.98°, 39.42°, 43.16°, etc. are indexed to the (012), (104), (006), (110), (113), (202) Miller planes, respectively. Likewise, the dolomite peaks correspond
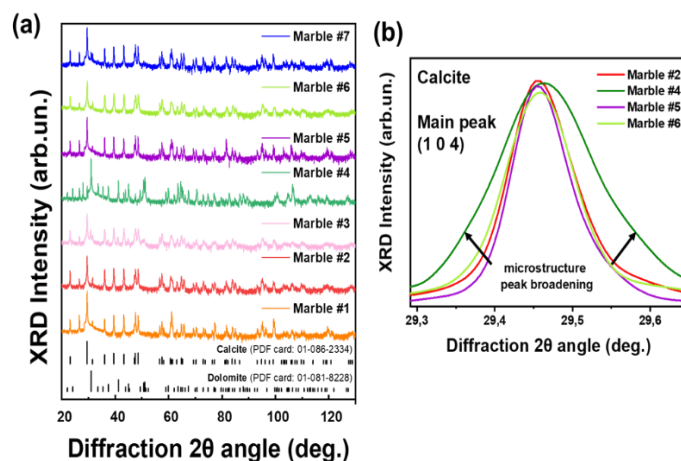

Figure 5 (**a**) XRD patterns from collected Greek marbles and their major crystal phases, i.e. dolomite and calcite. (**b**) Magnified region of the main peak (1 0 4) of the Greek marbles, demonstrating the peak broadening as the microstrain increases.

to its trigonal phase with a rhombohedral lattice system, a =

4.87 Å, b = 4.87 Å, and c = 16.19 Å (JCPDS Card No. 36-0426). The reflections centered at 24.04°, 30.94°, 33.54°, 35.32°, 37.38°, 41.13°, etc. with the corresponding (101), (012), (104), (006), (015), (110) Miller planes belong to dolomite. The XRD data for all calcined materials are shown in Figure S3 in the Supporting Information. In Table 4, the crystallite-size and phase composition are listed, as derived from analysis of the XRD data.. The pure calcitic marbles are #1, #2, #5, #6 and #7 which means the majority of their composition is calcite and they possess traces of magnetite, quartz, akermanite and ankerite. Marble #3 is calcitic with a 12% dolomite, marble #4 is pure dolomitic with an infinitesimal $CaCO_3$ percentage of 3%.

Table 4. XRD analysis, crystallite-size and phase-composition of the studied marbles.

Marble	Grain size d_{XRD} (μm)		Phase composition (%) (± 0.5%)					
	Calcite $CaCO_3$	Dolomite $CaMg(CO_3)_2$	Calcite $CaCO_3$	Dolomite $CaMg(CO_3)_2$	Magnetite Fe_3O_4	Quartz SiO_2	Akermanite $Ca_2Mg(Si_2O_7)$	Ankerite $Ca(Fe,Mg,Mn)(CO_3)_2$
#1	2.80 ± 0.27	–	95	–	–	5	–	–
#2	2.82 ± 0.12	–	96	–	1	1.5	1.5	–
#3	1.94 ± 0.12	2.63 ± 0.61	83	12	–	2	2	1
#4	2.81 ± 0.11	1.91 ± 0.16	3	96	–	1	–	–
#5	1.54 ± 0.14	–	96	–	–	4	–	–
#6	1.91 ± 0.12	–	95.5	–	–	2.5	1	1
#7	1.91 ± 0.16	–	94	–	1	2.5	2.5	–

Table 5 lists the derived microstrain values (ε_0) from analysis of the XRD data. In all cases the macrostrains are in the range $\varepsilon_0 = 3–11 \times 10^{-4}$.

Table 5. Microstrain (ε_0) of the marbles obtained by analysis of the XRD data.

Marble	Microstrain ε_0 ($\times 10^{-4}$)	
	Calcite CaCO$_3$	Dolomite CaMg(CO$_3$)$_2$
#1	4.1 ± 0.7	–
#2	4.7 ± 0.2	–
#3	7.1 ± 0.6	11.4 ± 1.1
#4	8.6 ± 0.4	9.6 ± 0.6
#5	2.9 ± 0.3	–
#6	4.0 ± 0.2	–
#7	3.2 ± 0.4	–

In Figure 8 we present correlation plots of the lattice-microstrain values (ε_0) derived from XRD vs. the D and D$_{strain}$ values derived from EPR. We see that the microstrain ε_0 increases at marbles #3, #4 where dolomite or akermanite phases i.e., Mg atoms are introduced in the crystal phase. When we examine the correlation trends (D$_{strain}$ vs. ε_0) and (D vs. ε_0) in Figure 8a and 8b, we observe a diaspora of the points: marble #7 with its two ^{55}Mn D$_{strain}$ values is clearly identified at the left-hand part of Figure 8b. Marble #4 with its two species of ^{55}Mn^{2+}, D and D$_{strain}$ values is classified at the upper and lower parts of Figure 8a. Marble #1 with its two calcitic ε_0 values is associated at the middle parts of Figure 8a and 8b. More specifically, Marble #4 where dolomite is 96% and calcite is 4%, has a low ZFS D-value of 12Gauss while all marbles with more than 83% of calcite have a D range from 80Gauss up to 110Gauss. Microstrain analysis shows that all marbles with more calcite than dolomite phase composition, are in the range of 2.8×10^{-4} up to 7.5×10^{-4}. Regarding the D$_{strain}$ versus microstrain ε_0, we observe similar correlation i.e., for small microstrain values $\varepsilon_0 < 8.0 \times 10^{-4}$ we have calcitic marbles while for

large $\varepsilon_0 > 8.0 \times 10^{-4}$ we have the interference of dolomite. The D$_{strain}$ for pure calcitic marbles has the range of 0-30 G, whilst the dolomitic marbles have small range of 10-20 G.

Conclusions

A novel methodology is suggested which correlates magnetic resonance properties with crystal-microstrain in order to reveal a trend that reflects the provenance of the marble. Greek marbles from different places along Greece, have been selected according to their historical importance, provenance and studied using our EPR, ssNMR and XRD methods. Theoretical simulation of the EPR spectra using the Spin-Hamiltonian formalism, provides numerical values of the Zero Field Splitting tensor (D-tensor) and its D$_{strain}$ for each marble. High-Temperature EPR provides, fort the first time to our knowledge, important insight into the structural behavior of marble sunder heat-stress that can be related to environmental events through history. Marbles with different phase composition, i.e., calcite and dolomite, show an increment of D$_{strain}$ versus temperature. A pattern for marbles with more than 95% calcite is emerging which indicates a considerable D$_{stain}$ for 12 Gauss up to 47 Gauss versus temperature of 700K. On the other hand, dolomitic marble #4 show a lower range of D-tensor form 10Gauss το 20 Gauss. XRD shows that calcitic marbles have low microstrain (ε_0), whilst the dolomitic ones have larger lattice-microstrain (ε_0) which indicates that the interference of Mg atoms (marbles #3 and #4) into the carbonate lattice affects the local crystal environment enhancing the lattice distortions. Finally, we propose a correlation plot between lattice-microstrain (ε_0) and the D-tensor strain from XRD-data and EPR data, respectively. We consider that this correlation-tool can be of broader use i.e., to other marbles, as well as other cultural materials including ceramics and glasses with specific aims at deciphering the provenance and possibly historical path.
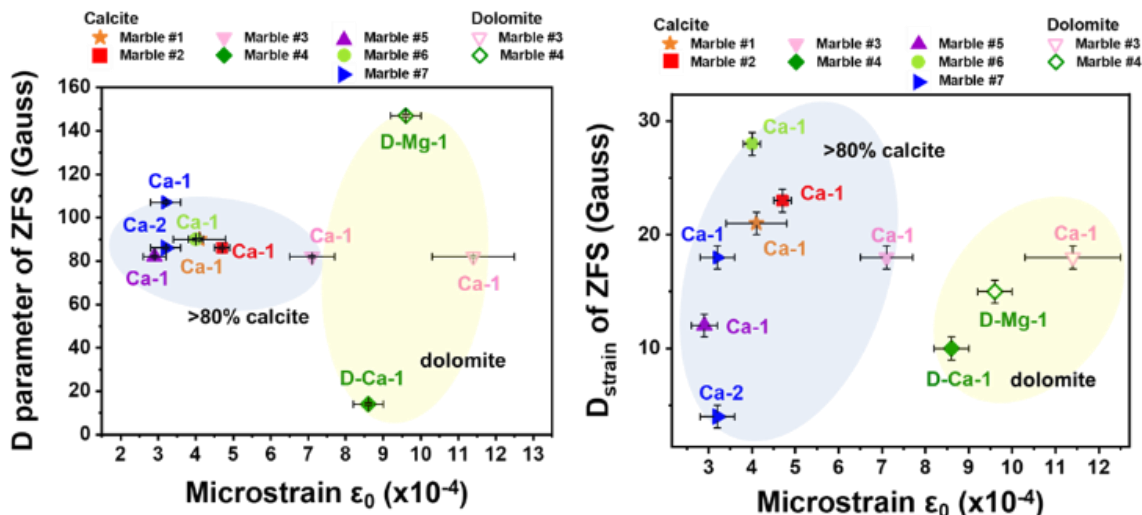

Figure 7 Correlation plot ZFS-XRD microstrain. (a) D axial parameter versus XRD-microstrain ε_0 and (b) D$_{strain}$ versus XRD-microstrain ε_0 for all the Greek marbles. We observe that when the marble is calcitic is positioned inside the blue bubble in the graph, while the dolomitic marbles are located in the yellow bubble. The points are notated as follows: Ca-1 for one species of calcite, Ca-2 for second species of calcite, D-Ca-1 for one species of calcite in dolomitic marble and D-Mg-1 for one species of dolomite in dolomitic marble (see Figure 4b).

Conflicts of interest

There are no conflicts to declare.

Acknowledgements

Notes and references

1 M. Waelkens, N. Herz, L. Moens and Association for the Study of Marble and Other Stones used in Antiquity, Eds., Ancient stones: quarrying, trade and provenance: interdisciplinary studies on stones and stone technology in Europe and Near East from the prehistoric to the early Christian period, Leuven University Press, Leuven, Belgium, 1992.

2   W. Prochaska and D. Attanasio, J. Archaeol. Sci. Rep., 2021, 35, 102676.

3   Y. Maniatis, D. Tambakopoulos, L. Lazzarini and M. C. Sturgeon, Archaeometry, 2021, 63, 685–704.

4   D. Attanasio, M. Bruno, W. Prochaska and A. B. Yavuz, Archaeometry, 2015, 57, 217–245.

5   K. Polikreti and Y. Maniatis, Archaeometry, 2002, 44, 1–21.

6   V. Baïetto, G. Villeneuve, M. Schvoerer, F. Bechtel and N. Herz, Archaeometry, 1999, 41, 253–265.

7   N. Herz and E. Garrison, in Treatise on Geochemistry, Elsevier, 2014, pp. 241–253.

8   D. Attanasio, R. Platania and P. Rocchi, J. Archaeol. Sci., 2005, 32, 311–319.

9   K. Polikreti and Y. Maniatis, Atmos. Environ., 2004, 38, 3617–3624.

10 I. Badouna, P. Koutsovitis, C. Karkalis, K. Laskaridis, N. Koukouzas, P. Tyrologou, M. Patronis, C. Papatrechas and P. Petrounias, Minerals, 2020, 10, 507.

11 G. Charalampides, N. Arvanitidis, K. I. Vatalis and S. Platias, Procedia Econ. Finance, 2013, 5, 143–151.

12 K. Al-Bashaireh, J. Archaeol. Sci. Rep., 2021, 35, 102777.

13 L. Moens, J. De Rudder, P. De Paepe and M. Waelkens, Bull. Sociétés Chim. Belg., 2010, 95, 399–406.

14 G. Poretti, M. Brilli, C. De Vito, A. M. Conte, A. Borghi, D. Günther and A. Zanetti, J. Cult. Herit., 2017, 28, 16–26.

15 M. L. Gerdes, L. P. Baumgartner and J. W. Valley, J. Petrol., 1999, 40, 853–872.

16 P. Blanc, M. P. Lapuente Mercadal and A. Gutiérrez Garcia-Moreno, Minerals, 2020, 10, 381.

17 J. D. Lynn, in All Days, SPE, Al-Khobar, Saudi Arabia, 2011, p. SPE-149091-MS.

18 Y. Maniatis and V. Mandi, J. Appl. Phys., 1992, 71, 4859–4867.

19 A. Gutiérrez Garcia-M., M. C. Savin, N. Cantin, S. Boudoumi, P. Lapuente, R. Chapoulie and I. Pianet, Archaeometry, 2019, 61, 795–808.

20 I. Pianet, A. Gutiérrez Garcia-Moreno, M.-C. Savin, N. Frerebeau, J. Trebosc, P. Florian and M. P. Lapuente Mercadal, Materials, 2023, 16, 1468.

21 K. Polikreti, Archaeometry, 2007, 49, 603–619.

22 Y. Maniatis, V. Mandi and A. Nikolaou, in Classical Marble: Geochemistry, Technology, Trade, eds. N. Herz and M. Waelkens, Springer Netherlands, Dordrecht, 1988, pp. 443–452.

23 Maniatis Y., Proc. Int. Sch. Phys. LdquoEnrico Fermirdquo, 2004, 154, 179–202.

24 S. Khrissi, L. Bejjit, M. Haddad, C. Falguères, S. Ait Lyazidi and M. El Amraoui, IOP Conf. Ser. Mater. Sci. Eng., 2018, 353, 012013.

25 J. D. Rimstidt, A. Balog and J. Webb, Geochim. Cosmochim. Acta, 1998, 62, 1851–1863.

26 R. G. C. Bathurst, Carbonate sediments and their diagenesis, Elsevier, Amsterdam, 2d enl. ed., 1975.

27 D. Camuffo, M. Del Monte, C. Sabbioni and O. Vittori, Atmospheric Environ. 1967, 1982, 16, 2253–2259.

28 D. A. Brown, D. C. Kamineni, J. A. Sawicki and T. J. Beveridge, Appl. Environ. Microbiol., 1994, 60, 3182–3191.

29 B. Bakruddin and A. R. Sembiring, J. Inotera, 2019, 4, 79.

30 D. Covaci, C. Costea, D. Dumitras and O. G. Duliu, 2012, 8771.

31 G. A. Yakaboylu, N. Gupta, E. M. Sabolsky and B. Mishra, Int. J. Rock Mech. Min. Sci., 2020, 130, 104345.

32 J. R. Pilbrow, Appl. Magn. Reson., 1994, 6, 161–181.

33 J. R. Pilbrow and G. R. Hanson, in Methods in Enzymology, Academic Press, 1993, vol. 227, pp. 330–353.

34 G. H. Reed and G. D. Markham, in Biological Magnetic Resonance, eds. L. J. Berliner and J. Reuben, Springer US, Boston, MA, 1984, pp. 73–142.

35 S. Zheng, J.-W. Feng and G. E. Maciel, Energy Fuels, 2005, 19, 1201–1210.

36 K. Momma and F. Izumi, J. Appl. Crystallogr., 2008, 41, 653–658.

37 Rietveld Refinement: Practical Powder Diffraction Pattern Analysis using TOPAS, De Gruyter, 2018.

38 Y. Zhao and J. Zhang, J. Appl. Crystallogr., 2008, 41, 1095–1108.

39 D. Sanna, G. Delogu, M. Mulas, M. Schirra and A. Fadda, Food Anal. Methods, 2012, 5, 759–766.

40 S. Stoll and A. Schweiger, J. Magn. Reson., 2006, 178, 42–55.

41 C. R. Byfleet, D. P. Chong, J. A. Hebden and C. A. McDowell, J. Magn. Reson. 1969, 1970, 2, 69–78.

42 C. R. De Abreu, T. C. Cordeiro, A. A. G. Carrasquilla, E. S. De Souza and A. O. Guimarães, J. Pet. Sci. Eng., 2021, 203, 108847.

43 R. A. Shepherd and W. R. M. Graham, J. Chem. Phys., 1984, 81, 6080–6084.

44 C. Ionescu, V. Hoeck, C. Gruian and V. Simon, Appl. Clay Sci., 2014, 97–98, 138–145.

45 K. Beshah, C. Rey, M. J. Glimcher, M. Schimizu and R. G. Griffin, J. Solid State Chem., 1990, 84, 71–81.

46 V. J. Witherspoon, J. Xu and J. A. Reimer, Chem. Rev., 2018, 118, 10033–10048.

47 H. Nebel, M. Neumann, C. Mayer and M. Epple, Inorg. Chem., 2008, 47, 7874–7879.